Modeling of active control of external magnetohydrodynamic instabilities*

James Bialek,† Allen H. Boozer, M. E. Mauel, and G. A. Navratil
Department of Applied Physics and Applied Mathematics, Columbia University, New York, New York 10027

(Received 27 October 2000; accepted 26 December 2000)

A general circuit formulation of resistive wall mode (RWM) feedback stabilization developed by Boozer [Phys. Plasmas **5**, 3350 (1998)] has been used as the basis for the VALEN computer code that calculates the performance of an active control system in arbitrary geometry. The code uses a finite element representation of a thin shell structure in an integral formulation to model arbitrary conducting walls. This is combined with a circuit representation of stable and unstable plasma modes. Benchmark comparisons of VALEN results with large aspect ratio analytic model of the current driven kink mode are in very good agreement. VALEN also models arbitrary sensors, control coils, and the feedback logic connecting these sensors and control coils to provide a complete simulation capability for feedback control of plasma instabilities. VALEN modeling is in good agreement with experimental results on DIII-D [Garofalo *et al.*, Nucl. Fusion **40**, 1491 (2000)] and HBT-EP [Cates *et al.*, Phys. Plasmas **7**, 3133 (2000)]. VALEN feedback simulations have also been used to evaluate and optimize the sensor/coil configurations for present and planned RWM experiments on DIII-D. These studies have shown a clear advantage for the use of local poloidal field sensors driving a ''mode control'' feedback logic control loop and configurations which minimize the control coil coupling to the stabilizing resistive wall. © *2001 American Institute of Physics.* [DOI: 10.1063/1.1362532]

I. INTRODUCTION

Control of long-wavelength magnetohydrodynamic (MHD) instabilities using a conducting wall near the plasma boundary and application of external magnetic perturbations is one of the most important routes to improved reliability and improved performance of magnetic fusion confinement devices. Conducting walls are known to prevent or reduce the growth of harmful, long-wavelength MHD instabilities in tokamaks[1] and spherical tori,[2] and they are essential to the operation of reversed field pinches (RFPs)[3] and spheromaks. Most attractive fusion power scenarios require wall stabilization to reach high fusion power density and operate continuously with low recirculating power.[4–6] Long-wavelength modes are stabilized by close fitting conducting walls because wall eddy currents oppose the helical perturbations created by these instabilities. However, for slowly growing instabilities, passive wall stabilization will fail when the eddy currents decay due to the finite resistivity of the wall. This allows resistive wall modes (RWMs) to grow on the time scale of magnetic diffusion through the wall, τ_w. RWMs have been identified in RFPs[7,8] and in tokamaks.[9–14]

Since the initial observations in DIII-D of the effectiveness of wall stabilization, high-performance, wall-stabilized plasmas have been produced transiently which satisfy the requirements for attractive high-β steady-state tokamak operation.[12,15] However, the onset of the RWM has been observed to be the limiting factor in the lifetime and β achieved in DIII-D advanced tokamak regimes with low internal inductance[16,17] and in HBT-EP.[13] Two schemes to control the unstable RWM have been proposed: (1) the plasma rotation with respect to the walls can be maintained (e.g., with neutral beam injection);[18] and (2) a network of active feedback coils can be configured so as to simulate: (i) a perfectly conducting wall[19,20], or (ii) a ''fake'' rotating wall,[21] or (iii) to provide direct feedback on the RWM amplitude.[22,23] In DIII-D the plasma rotation is observed to slow down when $\beta > \beta^{\text{no wall}}$ resulting in the failure of passive rotational stabilization,[12] hence, the development of active feedback systems may be essential if these modes are to be controlled.

The computer code VALEN has been developed to predict the performance of active feedback systems. The code models arbitrary conducting walls via a finite element representation using a thin shell integral formulation. This yields a circuit representation of all conducting structures. VALEN has a circuit representation for stable, and unstable plasma modes, and also models arbitrary magnetic sensors, control coils, and simple power supplies. The ability to simulate the effect of various feedback strategies among the sensors, power supplies, and control coils provides a complete simulation capability to accurately model active control of external MHD instabilities.

In Sec. II A we briefly describe the techniques used to model arbitrary conducting structures. In Sec. II B we review the formulations used to model the plasma instability in a circuit representation. The plasma model is exact within an ideal MHD linear mode analysis. Although these techniques may be extended to model rotating plasma instabilities we limit this paper to nonrotating instabilities. A simple example

*Paper GI1 4, Bull. Am. Phys. Soc. **45**, 118 (2000).
†Invited speaker.

with one degree of freedom for each major component is presented in Sec. II C. Section II D indicates how VALEN brings these techniques together for addressing the general problem of active feedback control. In Sec. III we present a study that examines the passive stabilizing effect of a nearby conducting wall in a large aspect ratio tokamak comparing the predictions of the VALEN code with analytic calculations from the single mode model. In Sec. IV we present basic VALEN predictions for active feedback using the ''smart shell'' feedback logic. Section V discusses approaches to optimization of the feedback sensor/control coil configuration in the HBT-EP tokamak and in DIII-D. Conclusions are given in Sec. VI.

II. PHYSICS MODEL FOR ACTIVE FEEDBACK CONTROL

A. Circuit model for induced currents in conducting structures

The VALEN code models the induced currents in distributed conducting structures as a set of R-L circuit equations. This is similar to the SPARK[24] code. The formulation allows analysis in the time domain, and also provides eigenvalue and eigenvector information.

Fields and currents are assumed to be quasistatic, i.e., the circuit approximation is valid, and we ignore displacement currents. The distributed conducting structure is represented by a collection of simple elements. Within the conducting structure current density is expressed as

$$\mathbf{J}(\mathbf{r},t)=\sum_k I_k(t)\mathbf{w}_k(\mathbf{r}). \tag{1}$$

The divergence free shape/weight functions $\mathbf{w}_k(\mathbf{r})$ correspond to macroscopic loops of current, usually a circulating current in each element. The shape functions define closed vector paths with units of inverse area. When elements are in physical contact, adjacent element currents are shared resistively on the common edge or surface. The $I_k(t)$ have units of amperes and are functions of time. Our final circuit equations will be expressed in terms of these variables. This choice of basis functions guarantees that the resulting equations will satisfy current conservation, i.e., $\nabla\cdot\mathbf{J}=0$. If the global geometry is multiply connected a few special global loops of current may be required to complete the space of possible solutions. For example, in a complete toroidal shell two additional global loops of current are required, one for net poloidal current and another for net toroidal current.

In VALEN we use a thin shell approximation in which currents and fields are assumed to vary on a spatial scale much larger than the thickness of a typical conductor and no effort is made to model skin current penetration through the thickness of an element. Currents are assumed to be uniform through the thickness of these thin elements. The thin shell approximation is accurate if the conducting structures are thin compared to $1/k$ with k the wave number of the mode. This approximation is adequate for almost all existing experimental fusion devices. In this approximation the currents are analogous to a surface stream function, and are referred to as mesh currents.

The circuit equations can be derived by making standard substitutions into $\mathbf{E}+\dot{\mathbf{A}}+\nabla\phi=0$. Each term is expressed in terms of the mesh currents $I_k(t)$ and the basis functions from Eq. (1). We use Ohm's law, $\mathbf{E}=\eta\mathbf{J}$, the familiar expression

$$\mathbf{A}(\mathbf{r})=\frac{\mu_0}{4\pi}\int_{\mathrm{vol}'}\frac{\mathbf{J}(\mathbf{r}')}{|\mathbf{r}-\mathbf{r}'|}dv'$$

for the vector potential (which assumes the Coulomb gauge), multiply by $\mathbf{w}_i(\mathbf{r})$, and integrate over all space. This integral formulation gives the basic equation for distributed circuit analysis, Eq. (2), and the current distribution is now described in terms of mesh currents instead of field variables. The shape/weight functions $\mathbf{w}_k(\mathbf{r})$ essentially define finite elements

$$\int_{\mathrm{vol}}\mathbf{w}_i(\mathbf{r})\cdot\left(\eta\sum_k I_k(t)\mathbf{w}_k(\mathbf{r})+\frac{\mu_0}{4\pi}\int_{\mathrm{vol}'}\frac{\Sigma_k\dot{I}_k(t)\mathbf{w}_k(\mathbf{r})}{|\mathbf{r}-\mathbf{r}'|}dv'+\nabla\phi\right)dv=0. \tag{2}$$

Equation (2) produces the standard circuit equation for distributed conducting structures. Collecting terms dependent on $\dot{I}(t)$ and $I(t)$ we obtain

$$[L]\{\dot{I}(t)\}+[R]\{I(t)\}=\{V(t)\}. \tag{3}$$

Here the square brackets [ ] are used to represent matrices and the notation { } is used to represent a column vector. The inductance matrix $[L]$ has terms

$$L_{ij}=\frac{\mu_0}{4\pi}\int_{\mathrm{vol}}\int_{\mathrm{vol}'}\frac{\mathbf{w}_i(\mathbf{r})\cdot\mathbf{w}_j(\mathbf{r}')}{|\mathbf{r}-\mathbf{r}'|}dv'\,dv \tag{4}$$

and the resistance matrix $[R]$ is

$$R_{ij}=\int_{\mathrm{vol}}\eta\mathbf{w}_i(\mathbf{r})\cdot\mathbf{w}_j(\mathbf{r})dv. \tag{5}$$

These matrices are constants for a particular conducting structure. Equations (4) and (5) are generalizations of Neuman's formula for inductance, and the standard definition of lumped resistance. Since the basis functions are divergence free, the integral $\int_{\mathrm{vol}}\mathbf{w}_i(\mathbf{r})\cdot\nabla\phi dv=0$ in general. The right-hand side of Eq. (3), $\{V(t)\}$, is the applied voltage

$$V_i(t)=-\int_{\mathrm{vol}}\mathbf{w}_i(\mathbf{r})\cdot(\dot{\mathbf{A}}_{\mathrm{ext}}(\mathbf{r},t)+\nabla\phi)dv. \tag{6}$$

For example, if there are exterior sources of changing magnetic field then the applied (loop) voltage is $V_i(t)=-\int_{\mathrm{vol}}\mathbf{w}_i(\mathbf{r})\cdot\dot{\mathbf{A}}_{\mathrm{ext}}(\mathbf{r},t)dv$. If there are voltage power supplies present then $V_i(t)=-\int_{\mathrm{vol}}\mathbf{w}_i(\mathbf{r})\cdot\nabla\phi(t)dv=-\oint\phi(t)\mathbf{w}_i(\mathbf{r})\cdot d\mathbf{a}$ for those paths that pass through a voltage power supply.

B. Plasma circuit formulation

If a plasma instability is completely internal with no exterior magnetic signature, then feedback stabilization will not control the instability. When a plasma instability has an external magnetic signature, the external magnetic properties of a MHD perturbation are completely described by giving the

normal component of the magnetic perturbation at the location of the surface of the unperturbed plasma. The interaction of an external MHD instability with all surrounding conductors and coils may be modeled by representing the instability in terms of a scalar magnetic potential. The circuit model for the plasma instability has been formulated by Boozer.[22] This formulation was designed to combine with the circuit model used for distributed conducting structures described previously.

Let (ρ,θ,φ) be a set of toroidal coordinates in which the surface of the plasma is defined by ρ equal to a constant. The normal component of the magnetic field for the plasma instability may be written in terms of flux as $\mathfrak{J}\mathbf{B}\cdot\nabla\boldsymbol{\rho}=\Sigma\Phi_i(t)f_i(\theta,\varphi)$ with $\mathfrak{J}$ the Jacobian of the coordinate system. The eigenfunctions $f_i(\theta,\varphi)$ are chosen do diagonalize the operator,

$$\delta W=\frac{1}{2}\sum\ \varpi_i\Phi_i^2, \tag{7}$$

which gives the *change in the energy* in the region occupied by the plasma and a surrounding vacuum. The plasma perturbation is unstable in the presence of a conducting wall if any of the eigenvalues of δW, the ϖ_i, are negative. The eigenfunctions $f_i(\theta,\varphi)$ of δW are orthonormal $\int f_i f_j d\theta\, d\varphi=\delta_{ij}$. This implies that the Φ_i are given by $\Phi_i=\int f_i(\theta,\varphi)\mathbf{B}\cdot d\mathbf{a}$ where $d\mathbf{a}=\mathfrak{J}\nabla\rho d\,\theta d\varphi$.

The perturbed magnetic field outside a plasma can be defined by a surface current distribution on a control surface just outside the surface of the unperturbed plasma. The surface current distribution $\mathbf{K}(\theta,\varphi)$ may be obtained via the equations $\lfloor\mathbf{B}\cdot\nabla\rho\rfloor=0$ and $\nabla\times\lfloor\mathbf{B}\rfloor=\mu_0\mathbf{K}$, with $\lfloor\ \rfloor$ meaning the jump across the control surface. This surface current is divergence free and tangential to the control surface so it may be written as

$$\mathbf{K}=\nabla\kappa\times\nabla\rho\,\delta(\rho-\rho_s) \tag{8}$$

with

$$\kappa(\theta,\varphi,t)=\sum\ I_i(t)g_i(\theta,\varphi). \tag{9}$$

Each $g_i(\theta,\varphi)$ is chosen so the field it produces, in the absence of any other currents, is the normal field $\mathfrak{J}\mathbf{B}\cdot\nabla\rho=\Phi_i(t)f_i(\theta,\varphi)$. The Φ_i and the current I_i are proportional, so the effective inductance for a plasma perturbation may be defined by $\Phi_i=L_iI_i$. The surface current associated with the plasma perturbation is defined by a set of currents, I_i^p. Since I_i^n is proportional to the Φ_i,[22]

$$L_iI_i^p=\sum\ (\delta_{ij}+s_i\lambda_{ij})\Phi_j, \tag{10}$$

where s_i are constants such that $s_i=-\varpi_iL_i$, and $\lambda_{ij}^{-1}=\int f_ig_j d\,\theta d\,\varphi$. Equation (10) connects the stability of the plasma perturbations to the circuit equations that follow.

In standard MHD stability analysis the potential energy released by the instability is transferred into plasma kinetic energy. Growth rates of an instability are frequently estimated by finding the extremal value for the ratio of potential to kinetic energy. The use of kinetic energy as a sink for the potential energy is inconvenient in a study of wall modes. We use a dissipative shell lying on the surface of the plasma to serve this purpose. The current in the dissipative shell that is associated with a given mode has the spatial distribution, $g_i(\theta,\varphi)$ of Eq. (9), and an amplitude I_i^d. The current in the dissipative shell I_i^d is determined by Ohm's law,

$$d\Phi_i/dt=-R_iI_i^d, \tag{11}$$

with R_i an assumed resistivity in ohms for the dissipative shell. The value of R_i is chosen so R_i/L_i simulates the growth rate of the ideal mode. The total current I_i flowing in the surface current on the plasma boundary is the sum of the perturbed plasma current I_i^p and the current in the dissipative shell I_i^d,

$$I_i=I_i^p+I_i^d. \tag{12}$$

The effects of currents in walls and coils external to the plasma are important factors in the study of feedback stabilization. We define the *i*th component of the flux associated with an external magnetic field, $\mathbf{B}_{\text{ext}}$ by

$$\Phi_i^{\text{ext}}=\int f_i(\theta,\varphi)\mathbf{B}_{\text{ext}}\cdot d\mathbf{a} \tag{13}$$

evaluated on the plasma surface. The Φ_i^{ext} are proportional to the currents in the walls and coils I_j^w, and may be written in the form $\Phi_i^{\text{ext}}=\Sigma M_{ij}I_j^w$. The normal field on the plasma surface in each of the modes is given by the sum $\Phi_i=L_iI_i+\Phi_i^{\text{ext}}$, or

$$\Phi_i=L_iI_i+\sum\ M_{ij}I_j^w. \tag{14}$$

The wall or coil currents are also determined by Ohm's Law,

$$\frac{d\Phi_w}{dt}=-\sum\ R_{wk}I_k^w+V_w(t), \tag{15}$$

with the flux through the wall or coil circuits given by

$$\Phi_w=\sum\ L_{wk}I_k^w+\sum\ M_{wi}I_i, \tag{16}$$

and the applied voltage on the external coils (if any) specified by $V_w(t)$. These equations define the circuit model used in VALEN.

The plasma perturbation eigenfunctions are defined once Eq. (7) has been specified. At present only one plasma eigenfunction is used in VALEN—the eigenfunction associated with the least stable perturbation (most positive *s*). This is equivalent to assuming that the plasma perturbation mode structure is rigid, and only changes in amplitude and not in spatial form. It is planned to generalize VALEN to implement multiple plasma mode eigenfunctions. These additional eigenmodes can be excited by the feedback system and their inclusion would give an accurate response of the plasma to feedback. However, as noted by Okabayashi[25] the approximation of a rigid plasma perturbation (a single plasma eigenfunction) appears to be accurate for the plasmas such as those of the RWM studies in DIII-D.

C. Single mode example

Consider the idealized passive case, i.e., the interaction of a single plasma eigenmode with a wall. The response of the wall is approximated by one circuit, i.e., one current I^w. The strength of this eigenmode is characterized by I^w or the associated magnetic flux penetrating the wall, Φ_w. We characterize the plasma perturbation as a single current I^p with flux Φ. The perturbed plasma current, I^p, is determined by the stability equation, $LI^p=(1+s)\Phi$. On this same control surface there is also a current I^d, associated with the dissipative circuit. The total current in this surface is $I=I^p+I^d$. Collecting the expressions for magnetic flux in the wall, the normal field on the plasma (in terms of flux), and the stability equation,

$$\begin{aligned} &L_w I^w + M_{wp} I^d + M_{wp} I^p = \Phi_w, \\ &M_{pw} I^w + L I^d + L I^p = \Phi, \\ &L I^p (1+s) = \Phi, \end{aligned} \tag{17}$$

$$\begin{aligned} &\frac{d\Phi_w}{dt} + R_w I^w = 0, \\ &\frac{d\Phi}{dt} + R_d I^d = 0. \end{aligned} \tag{18}$$

Since the plasma perturbation flux Φ occurs in the second and third parts of Eq. (17) we may eliminate I^p and define a new pair of inductance equations that implicitly contain the stability equation from Sec. II B,

$$\begin{aligned} &\left(L_w - M_{wp} \frac{1}{L} \left(\frac{1+s}{s} \right) M_{pw} \right) I^w \\ &\quad + \left(M_{wp} - M_{wp} \frac{1}{L} \left(\frac{1+s}{s} \right) L \right) I^d = \Phi_w, \\ &\left(M_{pw} - L \left(\frac{1+s}{s} \right) \frac{1}{L} M_{pw} \right) I^w + \left(L - L \left(\frac{1+s}{s} \right) \frac{1}{L} L \right) I^d = \Phi, \end{aligned} \tag{19}$$

where, as before, $s=-\varpi L$.

When s is positive, the plasma perturbation produces an unstable mode in these circuit equations. The growth rate, ν, (inverse time constant) of the unstable eigenvalue characterizes the growth of the plasma instability in the presence of the conducting structure and is given by a quadratic dispersion relation:[22]

$$(1-C)\nu^2 + \gamma_d \Delta (1-C)\nu - \gamma_d \gamma_w = 0, \tag{20}$$

where $C=M_{pw}M_{wp}/LL_w$, $\Delta=[(C+\gamma_w/\gamma_d)/(1-C)]-s$, $\gamma_d=R_d/L\sim 1/\tau_{\text{Alfvén}}$, and $\gamma_w=R_w/L_w$. The key parameters are the normalized plasma–wall coupling, C, which varies from 0 to 1, the ideal mode Alfvénic growth rate, γ_d, and the resistive wall time scale, γ_w. Since $\gamma_d \gg \gamma_w$, the characteristic form of this dispersion relation is given in Fig. 1, showing a slowed growth rate, resistive wall mode branch at low values of s, and a transition to the Alfvénic ideal mode branch at $S_c=C/1-C$ corresponding physically to the maximum value of s stabilized by a perfect conducting wall where $\gamma_w \to 0$.

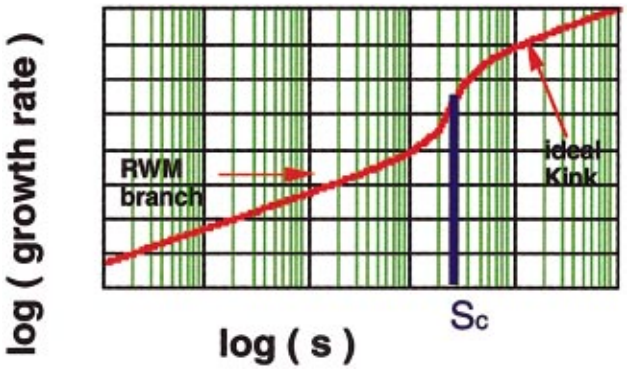

FIG. 1. (Color) Idealized, single mode, dispersion relation for the growth rate of the kink mode with a nearby resistive wall.

D. VALEN finite element implementation

VALEN implements the general formulation of the abovementioned problem. The complete problem may be thought of as a partitioned matrix circuit equation, Eq. (1). The stability matrix, $[S]$, comes from Eq. (10). The column vector $\{\Phi_s\}$ refers to the flux in sensor coils and $\{V_s\}=-\{\dot{\Phi}_s\}$ refers to the voltage in sensor coils,

$$\begin{aligned} &\begin{bmatrix} [L_w] & [M_{wp}] & [M_{wp}] \\ [M_{pw}] & [L_p] & [L_p] \end{bmatrix} \begin{Bmatrix} \{I^w\} \\ \{I^d\} \\ \{I^p\} \end{Bmatrix} \\ &\quad = \begin{Bmatrix} \{\Phi_w\} \\ \{\Phi\} \end{Bmatrix}, \quad \begin{aligned} &\{\dot{\Phi}_w\} + [R_w]\{I^w\} = \{V\}, \\ &\{\dot{\Phi}\} + [R_d]\{I^d\} = \{0\}, \end{aligned} \\ &\quad [L_p]\{I^p\} = [S]\{\Phi\}, \end{aligned} \tag{21}$$

where

$$S_{ij} = (\delta_{ij} + s_i \lambda_{ij}) \tag{22}$$

and

$$[[M_{sw}]\ [M_{sd}]\ [M_{sp}]] \begin{Bmatrix} \{I^w\} \\ \{I^d\} \\ \{I^p\} \end{Bmatrix} = \{\Phi_s\}. \tag{23}$$

The techniques described in Sec. II A have been implemented in VALEN to describe arbitrary thin shell conducting structures. Matrices $[L_w]$ and $[R_w]$ are defined by the techniques described in Sec. II A. Currents in all conducting structures are now essentially surface currents. Which is adequate for almost all existing plasma experiments. The conducting walls may be conformal to the plasma, nonconformal, partial walls (see Sec. III), or any combination of these options. Depending on the geometry of the conducting wall, several hundred to a couple of thousand elements have been used to model, respectively, HBT and DIII-D.

We use the same techniques to include control coils into the circuit model. A coil is treated as a global loop of current with specified cross-sectional area and resistivity. We also allow the possibility of sensor coils. Since a typical sensor

coil would have negligible current we exclude sensor coil currents from the eddy current formulation. This avoids numerical problems produced by great differences in current magnitudes. Sensor coils are included in the eddy current formulation only as a mutual inductance matrix $[[M_{sw}][M_{sd}][M_{sp}]]$ which has size number of sensors by the total number of currents, Eq. (22). In VALEN, the geometry of active coils or sensor coils is described by piecewise linear paths in space. The cross-sectional area, resistivity (for active coils), and number of turns must also be specified. $[M_{sw}]$ is derived by a straightforward application of Eq. (4).

The plasma perturbations representing the eigenfunctions of the operator δW must be supplied to VALEN. These eigenfunctions specify the external magnetic field and depend on typical plasma parameters such as current and pressure. DCON[26] produces this type of information. Usually stability codes calculate the most unstable eigenvector and its growth rate (eigenvalue). This is different from the desired eigenvectors of δW. Boozer argues that at the point of marginal stability, growth rate eigenvectors, which depend on a kinetic energy operator, approach arbitrarily closely to the eigenvectors describing the change in energy that VALEN requires. In this manner we have used input information from GATO[27] in some VALEN calculations. Other stability codes could also be used for VALEN input. When such an approach is taken we extrapolate the range of validity by the use of a qualitatively correct expression for the stability constant,

$$s \propto \frac{\langle\beta\rangle - \langle\beta\rangle_{\text{free}}}{\langle\beta\rangle_{\text{fixed}} - \langle\beta\rangle}. \tag{24}$$

Plasma perturbations need to be described in terms of the normal magnetic field on a control surface placed at the location of the unperturbed plasma. This information is then used to solve for a surface current distribution that best reproduces that normal magnetic field. Equation (4) is again used to define the self- and mutual inductances of the plasma perturbation. When using Eq. (4) in this situation, one of the shape functions represents the complete surface current distribution and the other shape function represents either a wall finite element, an active control coil, a sensor coil, or another complete surface current distribution.

As in the simple example given previously the stability information must be incorporated back into the inductance matrix. The stability matrix, $[S]$, is used to eliminate $\{I^p\}$ from the problem formulation. We substitute the following expression for $\{I^p\}$ into Eq. (20). This again incorporates all the stability information into the circuit equations,

$$\{I^p\} = ([S]^{-1}[L_p] - [L_p])^{-1}([M_{pw}]\{I^w\} - [L_p]\{I^p\}). \tag{25}$$

A very important aspect of the VALEN implementation is the ability to specify feedback strategy. In VALEN we have the ability to specify the voltage on any active coil. In general a coil forcing voltage has the following form:

$$V_c = \sum G^P_{ci}\Phi^S_i(t-\tau^P_{ci}) + \sum G^D_{ci}V^S_i(t-\tau^D_{ci}) + \sum G^P_{Ii}I_i(t-\tau^P_i) + \sum G^D_{Ii}\dot{I}_i(t-\tau^D_i), \tag{26}$$

where V_c is the applied voltage, Φ^S_i is a sensor flux, V^S_i is a sensor voltage, I_i and $\dot{I}_i$, are any current or its time derivative, G^P_{ci} and G^D_{ci} are the proportional or derivative gain in the active coil ''c,'' G^P_{Ii} and G^D_{Ii} are proportional or derivative gain for any current, and a time delay τ may be applied to any term. The gain terms have user specified characteristics. Current power supplies may be modeled as an extra feedback expression between power supply voltage and current through the power supply circuit.

If we limit ourselves to zero time delays and constant gains a feedback strategy may be studied as an eigenvalue problem in Eq. (3). For example, if all time delays in Eq. (24) are identically zero, and the gain coefficients are constants, then Eq. (22) may be used to express the sensor flux Φ^S_i and its time derivatives in terms of the $I_k(t)$ and its derivatives. In this situation, all these dependencies may be collected on the left-hand side of Eq. (3) to produce a well-defined eigenvalue problem. The unstable eigenvalues of this generalized circuit equation are reciprocal growth rates of the unstable modes.

All of these capabilities have been implemented using FORTRAN 90 and the Numerical Algorithms Library (NAG) mathematical library. The VALEN program is not a single executable code but rather a collection of several executable modules. For example, the first module computes the inductance and resistance matrix for all conductors and coils. A second module computes the additional inductance and resistance contributions from all the plasma modes. Other modules then are used to: (1) calculate transients in the time domain, (2) examine the eigenvalues and eigenvectors of the model, and (3) produce graphical summaries of the resulting current distributions.

III. VALEN PASSIVE STABILIZATION STUDIES AT LARGE R/a

Our first example of VALEN results uses the eigenvalue formulation described previously and examines the passive stabilization provided by a resistive wall concentric with a large aspect ratio, $R/a = 7.66$, circular cross-section plasma with minor radius a. The helical perturbation of the unstable mode describes an $m/n = 3/1$ external kink. The toroidal resistive wall (taken as a cylindrical aluminum wall, radius b and thickness 0.01 m) was examined for two plasma wall radii, one close to the plasma surface with $b/a = 1.08$ and the other relatively far away with $b/a = 1.7$. Figure 2 illustrates the results of this study as a plot of growth rate versus the strength of the unstable mode, s, as defined in Eq. (10). VALEN calculations show the characteristic two unstable branches (RWM and ideal kink) illustrated in Fig. 1 for the single mode analytic model. The expected result that stronger unstable modes (i.e., larger s) can be slowed to the RWM

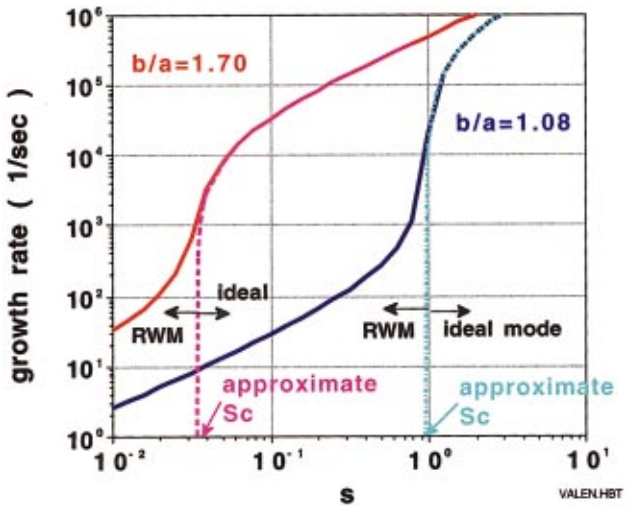

FIG. 2. (Color) VALEN calculation of the growth rate for an $m/n=3/1$ kink mode at large R/a surrounded by a concentric conducting wall at two normalized wall radii, b/a. Both the original plasma and the surrounding wall have a circular cross section. ''*a*'' is the plasma minor radius and ''*b*'' is the wall minor radius.

branch for a close fitting wall is clearly recovered, with the transition value of s identified as S_c=the stability limit for an ideally conducting wall.

In order to provide a quantitative benchmark for VALEN, we compare the values of S_c presented in Fig. 2 with the results of an analytic calculation of ideal wall stabilization based on a circular cross plasma for an ideal, current driven kink published by Wesson.[28] The circular cross-section plasma in the Wesson model has minor radius ''*a*,'' and the surrounding aluminum resistive wall was placed at two different radii, ''*b*.'' We see in Fig. 3 that the values of S_c from the VALEN calculation are in very good agreement with the values of S_c from the analytic Wesson model. The value of S_c is obtained from the Wesson calculation by estimating the value of s where the inflection point occurs in the growth rate. The value of S_c is obtained from the VALEN calculations by altering the wall resistivity to approximate a perfect conductor and then estimating the value of s where the inflection point occurs. In the VALEN results the region to the left of the appropriate blue curve have extremely slow growth rates and are essentially stabilized.

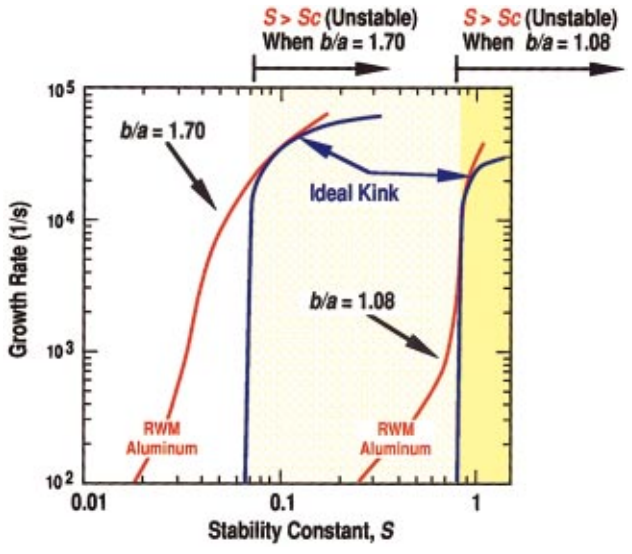

FIG. 3. (Color) Comparison of VALEN large R/a calculation of kink mode growth rate shown in Fig. 2 with an analytic result using the Wesson model. Both the original plasma and the surrounding walls have a circular cross section. ''*a*'' is the plasma minor radius and ''*b*'' is the wall minor radius. The VALEN results are shown in blue and the Wesson results in red. We compare the inflection point for the resistive Wesson model with the inflection point for the VALEN structure with approximate perfect conductivity.

An important feature of the VALEN code is that the wall need not be conformal or simply connected. To illustrate this capability, Fig. 4 summarizes the results for the situation where the $b/a=1.08$ and the 0.01-m-thick aluminum conformal wall modeled in Fig. 2 was cut into isolated segments. In one sequence of calculations, equally spaced poloidal cuts of 1°, 5°, and 10° toroidally were applied as shown schematically in the figure. In another sequence the inner 180° poloidally of the wall was removed and the same equally spaced poloidal cuts of 1°, 5°, and 10° toroidally were applied as shown schematically in Fig. 4. The VALEN calculation of the value of S_c for these configurations is plotted in Fig. 4 as a function of the fractional % of conducting wall area which remains for each configuration. We see that the relation between S_c and wall fraction is roughly linear. This result is to be expected since we are modeling a current driven kink at large aspect ratio which has little poloidal variation in mode amplitude. In the case of a lower aspect ratio beta driven kink with ballooning character the outer wall segments are seen to have a greater relative stabilizing effect.

IV. VALEN MODELING OF BASIC SMART SHELL STABILIZATION

Two approaches to active feedback control have been explored with the VALEN code: the ''smart shell'' and ''mode control.'' In the ''smart shell'' approach, originally proposed by Bishop[29] for the reversed field pinch, an externally generated radial magnetic field is applied by a control coil to the resistive stabilizing wall which cancels the unstable mode generated radial flux soaking through the resistive wall. In this way the response of a perfectly conducting wall is simulated. Alternatively, the ''mode control'' approach[22,23] to feedback control seeks to cancel out the radial mode flux at the plasma surface by application of an externally generated field proportional to the mode amplitude.

Boozer[22] showed that in the idealized limit of one equation for the plasma mode, one for the wall, and one for a single active feedback control coil, the dispersion relation for a plasma mode stabilized by a smart shell feedback scheme may be described by a quadratic dispersion relation. Here the sensor coil located on the resistive wall measures a radial flux, Φ_s, and this flux signal determines a voltage V_f applied to the active feedback control coil. If the single active feedback control coil has self inductance L_f, resistance R_f, $\gamma_f = R_f/L_f$, mutual inductance M_{wf} between the resistive wall and the control coil, mutual inductance M_{pf} between the plasma mode and the control coil, and a proportional gain G_p

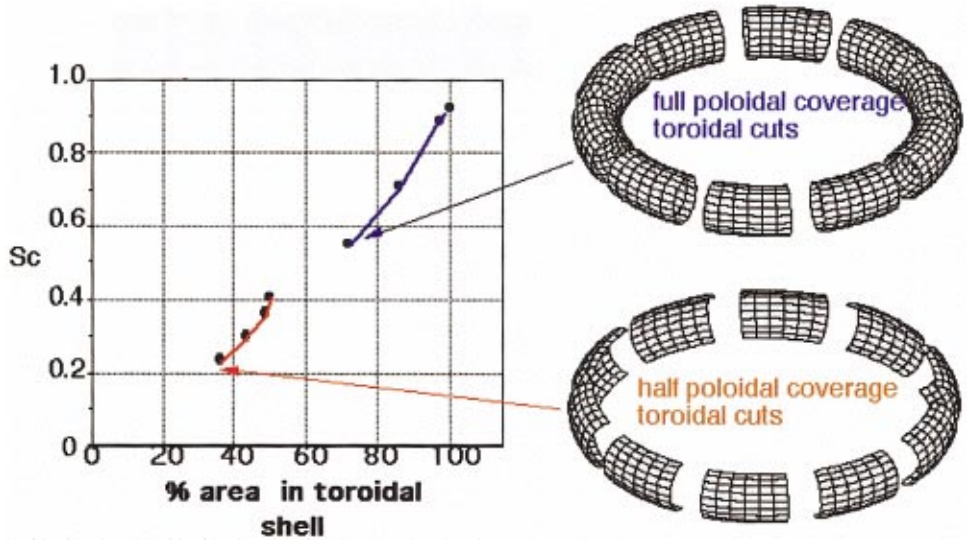

FIG. 4. (Color) VALEN model applied to a sequence of complex passive stabilizing structures for the kink mode of Fig. 2. with both toroidal and poloidal gaps in the conducting structure. The value of S_c as a function of % conducting wall coverage shows a roughly linear relation for this large aspect ratio geometry. Both the original plasma and the surrounding walls have a circular cross section.

so that $V_f = -L_f \gamma_w G_p \Phi_s / M_{pf}$ then the dispersion relation has the form

$$a_2 \nu^2 + a_1 \nu + a_0 = 0, \tag{27}$$

where $a_0/\gamma_f = -\gamma_f + \gamma_w (D + C_f) G_p$; $a_1 = D\gamma_f - \gamma_w$; and $a_2 = D$. The key parameters which characterize the active control system are the normalized coupling of the plasma mode to the wall, $C = M_{pw} M_{wp} / L L_w$, defined earlier and which varies between 0 and 1. A new parameter is the normalized feedback system coupling,

$$C_f = 1 - M_{pw} M_{wf} / L_w L_{pf},$$

which can be positive or negative, and the function $D(s) = [(1+s)C/s - 1]$ which is large and positive for small instability drive s, and decreases to 0 as s rises to ideal wall limit, S_c. Since $D(s) = a_2$ is positive on the RWM branch of the dispersion relation and the Hurwitz condition requires all coefficients, a_2, a_1, and a_0 to have the same sign to guaranty no unstable roots, this gives three conditions on the maximum value of s which can be stabilized by the active feedback system. The maximum stable values of s are set by the lowest of the three conditions,

$$a_2 > 0: \quad s < \frac{C}{1-C} = S_c, \tag{28}$$

$$a_1 > 0: \quad s < \frac{C}{1 - C + \gamma_w/\gamma_f} < S_c, \tag{29}$$

$$a_2 > 0: \quad s < \frac{C}{1 - C - C_f + [\gamma_f/\gamma_w] G_p^{-1}}. \tag{30}$$

The first condition of Eq. (28) limits us to stabilization up to the ideal wall limit. The second condition of Eq. (29) only approaches the ideal limit if the response time of the feedback system, L_f/R_f, is much faster than the resistive wall time constant L_w/R_w. The third condition of Eq. (30) shows that the effect of large values of proportional gain saturates as $G_p \to \infty$ and that s can approach S_c only if $C_f > 0$. Since in the case of a typical ''smart shell'' configuration the control coils are located outside the vacuum vessel wall and hence are coupled more strongly to the vessel wall than the plasma mode, C_f is usually negative and this condition sets the limit on basic smart shell performance.

The VALEN code was applied to modeling the basic feedback control performance of the three-dimensional smart shell configuration in the HBT-EP tokamak,[13,30] which is shown in Fig. 5. The system in HBT-EP uses a resistive stabilizing shell which is cut into ten 26° wide toroidal segments covering only roughly the outer 180° of the poloidal cross section. In feedback studies five of these wall segments are thick aluminum and are withdrawn far from the plasma and the other five thin stainless-steel segments ($\tau_w \sim 0.3$ ms) are placed at $b/a = 1.08$ and have been fitted with 30 independent sensor/control coil pairs as shown in the Fig. 5. Shown in Fig. 6 is a summary of the VALEN modeling of this HBT-EP smart shell active feedback system for three different gains, G_p, and compared with the result if the stainless-steel wall segments were perfect conductors. We see that these results are in good agreement with the analytic model described previously. First, we note that the application of feedback gain not only reduces the growth rate but actually fully stabilizes the RWM. Second, the effect of gain saturation is readily apparent as G_p is increased from 5×10^4 to 1×10^5 V/W. Finally, we note that the largest value of s which is stabilized is smaller than the S_c result for a perfect conductor, in agreement with Eq. (30), since the value of C_f for the HBT-EP smart shell configuration is less than 0 due to strong control coil/wall coupling.

Experiments using this HBT-EP smart shell configuration to stabilize the RWMs have been reported by Cates *et al.*[13] and showed that the gain required in the experiment to achieve RWM suppression was in good agreement with the VALEN model result of 10^5 V/W.

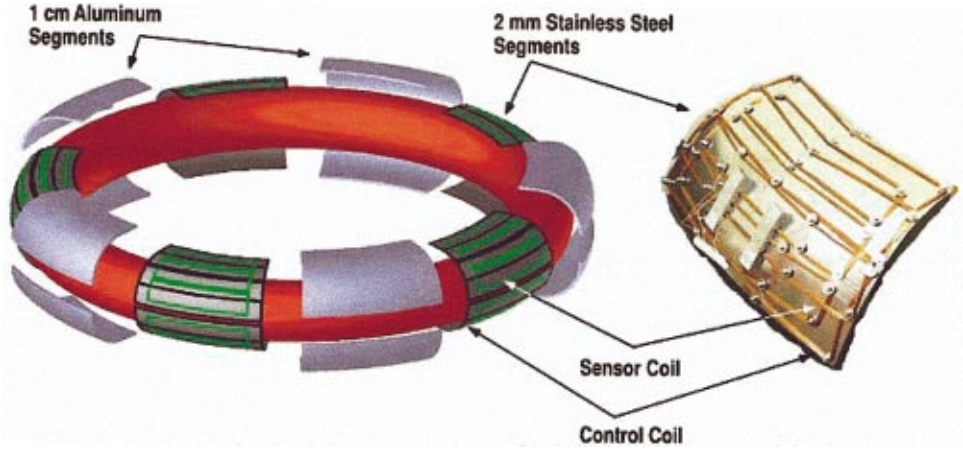

FIG. 5. (Color) Smart shell feedback control system in the HBT-EP experiment.

V. VALEN MODELING OF OPTIMIZED FEEDBACK CONFIGURATIONS

Following on the initial success reported in stabilizing the RWM with active feedback control on HBT-EP[13] and in DIII-D,[17,31] the VALEN code has been used to explore optimization of the feedback configuration on both devices with the objective of finding configurations and feedback algorithms which are projected to stabilize the RWM at the highest values of s and approaching as close as possible to the ideal wall beta limit, S_c. Examples of design choice issues for the ''smart shell'' configuration include: extent of poloidal coverage of radial flux sensors; optimal number of control coils and sensors, optimal sensor locations, and optimal size for sensors. In the case of application of the ''mode control'' approach to feedback, it is critical to obtain a high accuracy measure of the RWM amplitude and phase to be the input into the active feedback loop. One promising approach has been found to be the use of multiple poloidal magnetic field, B_p, sensor coils to identify amplitude and phase and to use midplane B_p sensors to minimize inductive coupling to the control coils. This scheme for ''mode control'' was also studied systematically with VALEN.

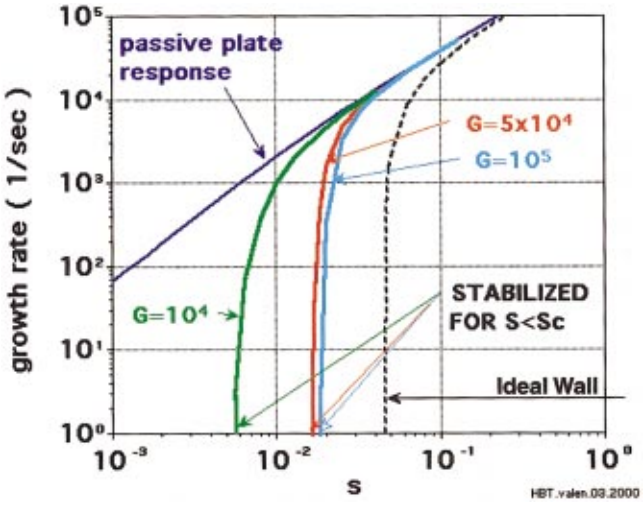

FIG. 6. (Color) VALEN calculation of basic smart shell stabilization in the geometry of HBT-EP using proportional gain, G_p, feedback.

In the context of DIII-D the performance of the basic ''smart shell'' feedback scheme with proportional gain was studied. Shown in Fig. 7 is a summary of a systematic study of the effect of adding additional poloidal segments of sensor/control coils to provide more complete coverage of the resistive vacuum vessel wall ($b/a \sim 1.3$ and $\tau_w \sim 5$ ms) which provides stabilization of the ideal $n=1$ external kink. The unstable RWM structure used in these studies was taken from a GATO calculation of the RWM instability in DIII-D shot number 92544. The feedback control coils presently installed on DIII-D consist of a single poloidal segment of six 60° wide control coils on the midplane located outside the toroidal field coils. Six radial flux sensors are mounted on the DIII-D vacuum vessel each directly under the radial footprint of one of the control coils. In these studies, additional polidal segments of six control coils and six sensors were added

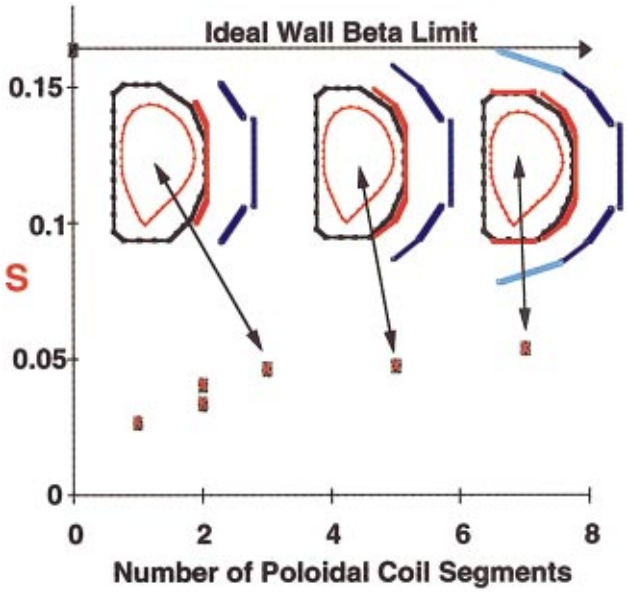

FIG. 7. (Color) VALEN calculation of effect of additional poloidal segments of feedback sensor/control coil elements in DIII-D for a smart shell with proportional gain feedback, showing that improvements in the maximum stable value of s saturate after about three segments. Each blue line segment is a set of six control segments and each exterior red line segment is a set of six radial flux sensors.

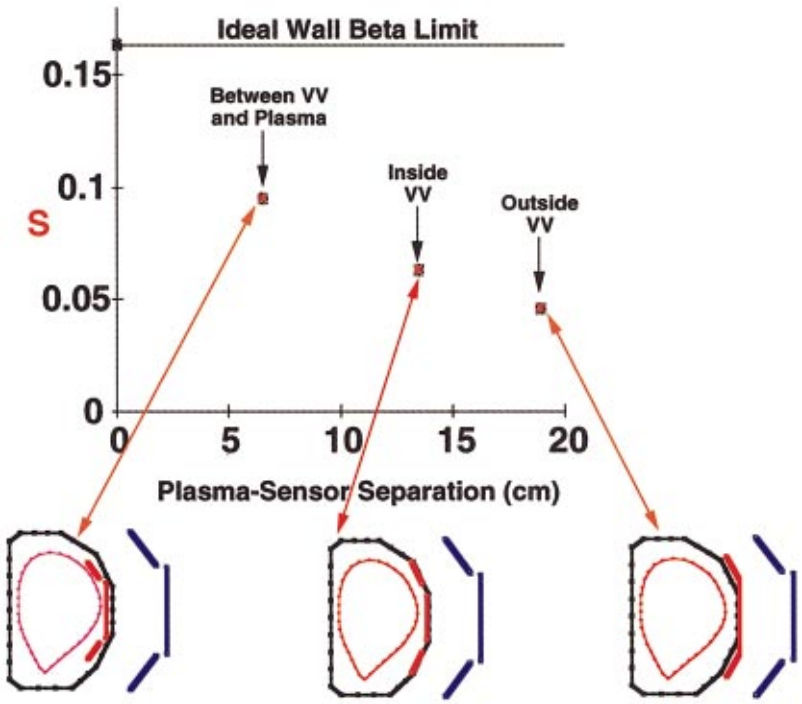

FIG. 8. (Color) VALEN calculation showing the effect of varying the distance between the plasma surface and radial flux sensors. The outermost segment of the vacuum vessel is located at $R=2.445$ m. The midplane ''outside VV'' sensors are located at $R=2.474$ m ($z=\pm 0.599$ m), midplane ''inside VV'' sensors are located at $R=2.420$ m ($z=\pm 0.420$ m), and midplane ''sensors between VV and plasma'' are located at $R=2.350$ m ($z=\pm 0.510$ m). The maximum radius of the plasma surface is 2.285 m.

vertically above and vertically below the midplane as shown schematically in Fig. 7. In Fig. 7 the icons illustrate 3, 5, and 7 poloidal segments for the control coils and radial flux sensors. Each straight line segment in blue represents an active control coil segment and each exterior straight line segment in red represents a radial flux sensor segment. We see that the addition of either a single segment vertically above or below the present single midplane segment improves the maximum stable value of s, and that further improvement is obtained with two additional segments, one above and one below the midplane segment for a total of 3 segments consisting of 18 sensor/control coil pairs. The addition of more segments up to a total of 7 showed relatively little additional improvement in the maximum stable value of s. Since the RWM induced eddy currents in the vacuum vessel wall are largest on the outboard midplane and diminish significantly on the top and bottom of the vacuum vessel due to the strong ballooning nature of the mode structure, this result is not unexpected.

Further optimization studies in the smart shell feedback scheme show little benefit for the addition of finer scale toroidal segmentation in the control coils which make up the additional poloidal segments. There was also no benefit observed to having the toroidal segments rotated in angle relative to the six control coils in the midplane poloidal segment. However, there was significant improvement in projected performance when the radial field flux sensors were ''shortened'' to subtend a smaller poloidal angle by providing a better mode amplitude signal with less averaging of the poloidal mode structure.

Using this optimal configuration of three poloidal segments consisting of 18 control coils outside the toroidal coils structure, the location of the 18 sensor loops, which measure radial flux, was varied in the VALEN modeling of basic smart shell performance with proportional gain for three sensor radial positions as shown in Fig. 8. It is clear from the results in Fig. 8 that significant improvements in the maximum stable value of s are possible if the sensors are located as close to the plasma surface as possible.

Additional improvements in projected feedback control performance in DIII-D are found when the mode control feedback scheme is modeled. Mode control uses tiny B_p sensor coils located on the outboard midplane just inside the vacuum vessel wall. Since these coils have nearly zero mutual inductive coupling to the control coils, they provide a high quality measure of the unstable RWM amplitude and phase. VALEN modeling of this feedback scheme showed dramatically improved performance relative to that obtained with the smart shell approach using B_r flux sensors near the vacuum vessel wall.

The results of these optimization studies in DIII-D for both single poloidal segment (6 control coils) and three poloidal segment (18 control coils) are summarized in Fig. 9. The results of the VALEN model are plotted with s mapped to β using the approximate relation given in Eq. (24), and normalized to the difference between the ideal wall β limit ($s=S_c$) and the no-wall beta limit ($s=0$). For the present control coils geometry of six midplane coils on DIII-D, we see the projected performance of the existing system with a basic smart shell feedback scheme with proportional gain limited to improving β to about 20% toward the ideal wall β limit, consistent with the modest feedback performance reported for this system on experiments showing RWM control on DIII-D.[17] The use of shorter sensors located inside the vacuum vessel and the existing six control coil system projects improvements to about 30% toward the ideal wall β limit. And the use of a toroidal array of midplane mounted B_p sensors improves the projected performance of the exist-

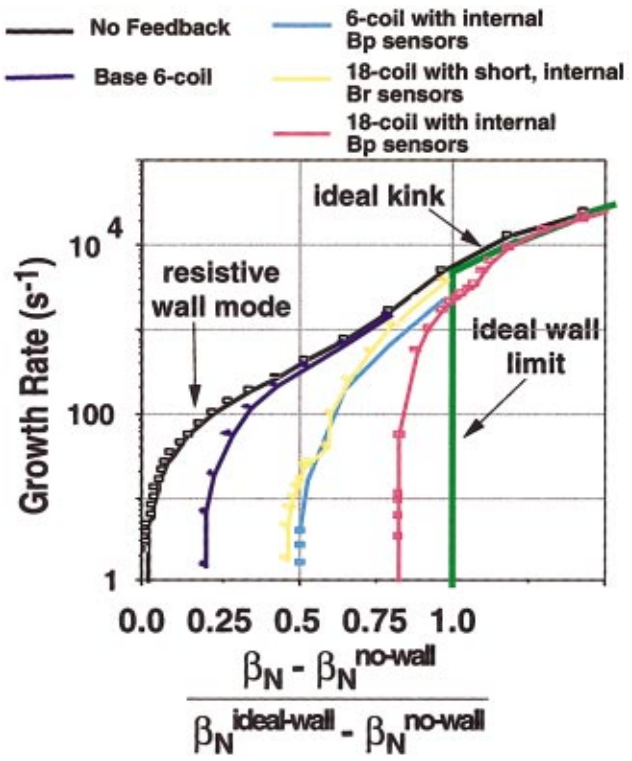

FIG. 9. (Color) Summary of VALEN calculations of optimized feedback configurations in DIII-D for both smart shell and mode control feedback logic.

ing six control coil set further to about 50% toward the ideal wall β limit. For an 18 control coil set in three poloidal segments which is proposed for future installation on DIII-D, the basic smart shell projected performance is improved to 50% toward the ideal wall β limit, while the use of a toroidal array of midplane mounted B_p sensors improves the projected performance of an 18 control coil set further to about 80% toward the ideal wall β limit.

Finally, a study of optimal feedback configurations for the HBT-EP tokamak investigated changes in control coil geometry which would minimize the inductive coupling between the control coils and the passive stabilizing wall, M_{wf}, while maintaining strong control coil coupling to the plasma, M_{pf}. In this way the normalized feedback coupling coefficient, $C_f = 1 - M_{pw}M_{wf}/L_wL_{pf}$, in the single mode model [Eq. (27)] can be made greater than 0 allowing the maximum value of s to approach the ideal wall limit, S_c. Shown in Fig. 10 is a proposed improved feedback control geometry for HBT-EP. Five of the thick aluminum segments are withdrawn and the control coils are moved into these toroidal gaps. The five passive stainless steel stabilizing wall segments (shown shaded) still have B_r flux sensors mounted on the back of these remaining wall segments. Also shown in Fig. 10 are the results of several VALEN calculations. The ''No Feedback'' curve is a prediction for passive stabilization in the existent HBT-EP geometry (five close fitting stainless steel passive segments). The curve labeled ''Present HBT-EP'' illustrates the best smart shell performance predicted for the existent geometry. The curve labeled ''Minimum M_{wf} Configuration'' illustrates the VALEN prediction for active control in the proposed improved geometry. Finally the curve labeled ''Ideal wall β limit'' illustrates the VALEN prediction for the passive stabilization that would be produced by the configuration where all ten passive stabilizing wall segments in the existing HBT-EP configuration are as close as possible to the plasma and approximate perfect conductors. The projected maximum stable value of s for the proposed active feedback configuration is very close to the ideal wall limit S_c for a configuration with ten passive stabilizing wall segments. This result is in agreement with predictions of the single mode analytic model.

VI. CONCLUSIONS AND FUTURE PLANS

The VALEN code has been developed as a tool to provide a complete simulation capability for feedback control of long-wavelength external MHD plasma instabilities in arbitrary three-dimensional geometry of passive resistive wall stabilizers, sensor coils, control coils, and feedback logic. Predictions of the VALEN code for passive stabilization have been benchmarked qualitatively against single mode analytic model of the RWM and quantitatively against Wesson's analytic model of a large R/a current driven kink mode. The VALEN model is also in good qualitative agreement with the

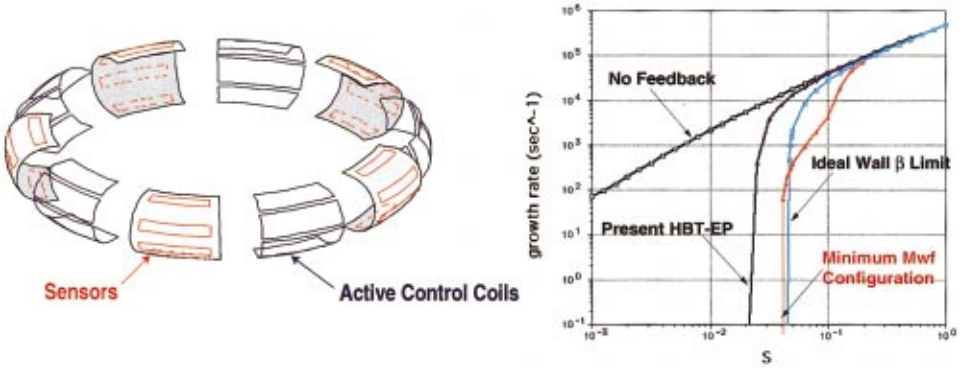

FIG. 10. (Color) VALEN calculation of a proposed feedback configuration in HBT-EP which minimizes the control coil–wall coupling allowing stabilization up the ideal wall limit of s. The curves labeled ''No Feedback'' and ''Present HBT-EP'' illustrate the VALEN predictions for passive and active performance in the existent HBT-EP. The curve labeled ''Minimum M_{wf} Configuration'' illustrates the VALEN prediction for the proposed configuration illustrated. The curve labeled ''Ideal wall β limit'' is the VALEN prediction for perfect conducting plates as close to the plasma as possible in all possible locations (see Fig. 5).

predictions of the analytic single mode model for basic smart shell feedback stabilization, and qualitative agreement with the experimental results on RWM feedback control reported for the HBT-EP tokamak[13] and DIII-D.[17,27]

The VALEN code has been used to model improved feedback control configurations for both HBT-EP and DIII-D with projected performance for both systems approaching the ideal wall stability limit. For the smart shell feedback approach, factors which were found to result in significant improvement in feedback performance included better coverage on the outboard vacuum vessel (passive stabilizing wall) area where the RWM induced eddy currents are largest, location of B_r flux sensors closer to the plasma surface, and reduction in the poloidal angle subtended by B_r flux sensors. For the mode control feedback approach factors which were found to result in significant improvement in feedback performance included better coverage on the outboard vacuum vessel (passive stabilizing wall) area where the RWM induced eddy currents are largest, the use of midplane B_p sensor coils with minimal inductive coupling to the control coils, and minimization of the control coil coupling to the passive stabilizing wall. For the mode control approach performance is projected to approach the ideal wall stability limit in optimized configurations for both HBT-EP and DIII-D.

In the present application of the code a single mode is used. This approximation appears to be accurate as reported by Okabayashi.[25] In the future we plan several improvements in the VALEN model to better model additional realistic effects in feedback applications. These include: (i) the addition of multiple plasma modes to investigate possible destabilization of other, near-marginal modes and to allow for possible changes in the plasma mode structure under application of feedback control, (ii) the addition of plasma rotation to the unstable plasma model in VALEN as formulated by Boozer;[32] and (iii) realistic nonideal feedback amplifier characteristics.

ACKNOWLEDGMENTS

We would like to thank PPPL and General Atomics for their support of this work as part of the RWM collaboration on the DIII-D National Fusion Facility. We also gratefully acknowledge useful discussion and input from R. Fitzpatrick, A. M. Garofalo, T. H. Jensen, R. J. Lahaye, M. Okabayashi, S. Sabbagh, E. J. Strait, T. Taylor, and A. D. Turnbull.

This work was supported by the United States Department of Energy.

[1] E. J. Strait, Phys. Plasmas **1**, 1415 (1994).
[2] T. C. Hender, S. J. Allfrey, R. Akers *et al.*, Phys. Plasmas **6**, 1958 (1999).
[3] H. A. B. Bodin, Nucl. Fusion **30**, 1717 (1990).
[4] A. D. Turnbull, T. S. Taylor, Y. R. Lin-Liu, and H. St. John, Phys. Rev. Lett. **74**, 718 (1995).
[5] C. Kessel, J. Manickam, G. Rewoldt, and T. M. Tang, Phys. Rev. Lett. **72**, 1212 (1994).
[6] R. L. Miller, Y. R. Lin-Liu, A. D. Turnbull, V. S. Chan, L. D. Pearlstein, O. Sauter, and L. Villard, Phys. Plasmas **4**, 1062 (1997).
[7] B. Alper, Phys. Fluids B **2**, 1338 (1990).
[8] P. Greene and S. Robertson, Phys. Fluids B **5**, 556 (1993).
[9] E. J. Strait, T. S. Taylor, A. D. Turnbull, L. L. Lao, B. Rice, O. Sauter, S. J. Thompson, and D. Wroblewski, Phys. Rev. Lett. **74**, 2483 (1995).
[10] T. H. Ivers, E. Eisner, A. Garafalo *et al.*, Phys. Plasmas **3**, 1926 (1996).
[11] M. Okabayashi, N. Pomphrey, and J. Manickam, Nucl. Fusion **36**, 1167 (1996).
[12] A. M. Garofalo, A. D. Turnbull, E. J. Strait *et al.*, Phys. Plasmas **6**, 1893 (1999).
[13] C. Cates, M. Shilov, M. E. Mauel, G. A. Navratil, D. Maurer, S. Mukherjee, D. Nadle, J. Bialek, and A. Boozer, Phys. Plasmas **7**, 3133 (2000).
[14] S. Takeji *et al.*, *IAEA Fusion Energy Conference 2000, Sorrento, Italy, Paper EX7/01* (International Atomic Energy Agency, Vienna, 2000).
[15] E. J. Strait, L. L. Lao, M. E. Mauel *et al.*, Phys. Rev. Lett. **75**, 4421 (1995).
[16] C. C. Petty *et al.*, *27th EPS Conference on Controlled Fusion and Plasma Physics, Budapest, Hungary, 2000* (European Physical Society, Petit-Lancy, 2000).
[17] A. M. Garofalo, E. J. Strait, J. M. Bialek *et al.*, Nucl. Fusion **40**, 1491 (2000).
[18] A. Bondeson and D. J. Ward, Phys. Rev. Lett. **72**, 2709 (1994).
[19] C. M. Bishop, Plasma Phys. Controlled Fusion **31**, 1179 (1989).
[20] T. H. Jensen and R. Fitzpatrick, Phys. Plasmas **4**, 2997 (1997).
[21] R. Fitzpatrick and T. H. Jensen, Phys. Plasmas **3**, 2641 (1996).
[22] A. H. Boozer, Phys. Plasmas **5**, 3350 (1998).
[23] M. Okabayashi, N. Pomphrey, and R. E. Hatcher, Nucl. Fusion **38**, 1607 (1998).
[24] D. W. Weissenburger, Princeton Plasma Physics Laboratory Report No. PPPL-2494, January 1988. Available from the National Technical Information Service, 5285 Port Royal Road, Springfield, VA 22161.
[25] M. Okabayashi, J. Bialek, M. S. Chance *et al.*, Phys. Plasmas **8,** 2071 (2001).
[26] A. H. Glasser and M. S. Chance, Bull. Am. Phys. Soc. **42**, 1848 (1997).
[27] L. C. Bernard, F. J. Helton, and R. W. Moore, Comput. Phys. Commun. **24**, 377 (1981).
[28] J. Wesson, Nucl. Fusion **18**, 87 (1978).
[29] C. M. Bishop, Plasma Phys. Controlled Fusion **31**, 1179 (1989).
[30] M. K. V. Sankar, E. Eisner, A. Garofalo, D. Gates, T. H. Ivers, R. Kombargi, M. E. Mauel, D. Maurer, D. Nadle, G. A. Navratil, and Q. Xiao, J. Fusion Energy **12**, 303 (1993).
[31] J. L. Luxon and L. G. Davis, Fusion Technol. **8**, 441 (1985).
[32] A. H. Boozer, Phys. Plasmas **6**, 3180 (1999).